Check for updates

# Microwave hydrothermal synthesis of α-MnMoO₄ nanorods for high electrochemical performance supercapacitors

S. Jayasubramaniyan,[ab] S. Balasundari,[bc] P. A. Rayjada,[d] N. Satyanarayana[e] and P. Muralidharan ⓘD *[b]

Pristine α-MnMoO₄ nanorods were facilely prepared *via* co-precipitation (Cp) and microwave hydrothermal (MH) methods. X-ray diffraction (XRD) patterns showed pure monoclinic crystalline phase α-MnMoO₄ for the heat treated powder at 500 °C. Fourier Transform Infrared (FTIR) spectra showed that the chemical bond structure of α-MnMoO₄ corresponds to the strong vibrational modes of Mo–O–Mo, Mo–O and Mo=O. Raman spectra showed the structural bonding and crystalline nature of α-MnMoO₄. Field Emission Scanning Electron Microscope (FE-SEM) images exposed the nanorod shape of the α-MnMoO₄ powder, with diameters of ∼200 nm and lengths of ∼1.6 μm. Electrochemical studies of the Cp- and MH-MnMoO₄ nanorods with 2 M NaOH as the electrolyte showed specific capacitances of 143 F g⁻¹ and 551 F g⁻¹, respectively, at a 1 A g⁻¹ constant discharge current density. Cyclic voltammetric (CV) studies of the MH-MnMoO₄ nanorods at various scan rates revealed the presence of redox pairs, suggesting a pseudocapacitive nature. The structural stability at different current densities demonstrated the high rate performances and good reversible capacity retention of the calcined MH-MnMoO₄ nanorods. A cycling life stability study of MH-MnMoO₄ demonstrated a good capacity retention of 89% of the initial specific capacitance at 5 A g⁻¹ after 1000 cycles.

## 1. Introduction

Recently, the design and manufacture of systems from simple electronic devices to hybrid electric vehicles has demonstrated a great need for a huge quantity of efficient energy-producing, energy-absorbing, and energy-storage technologies. The essential sustainable energy storage devices are electrochemical capacitors or supercapacitors, which have established conversion systems, fast charge–discharge processes, enhanced cycle stability, and higher power and energy density than batteries.[1–4] Based on the charge storage mechanism, supercapacitors can be classified as electric double layer capacitors (EDLCs) and redox- or pseudocapacitors.[5] The EDLC function is to accumulate electrical charge by electrostatic separation of charges at electrode/electrolyte interfaces with reversible electrolyte ion movement. For pseudocapacitors, charge transfer occurs by

a fast reversible redox reaction and active ion interactions at the electrode surface results in fast charge–discharge rates.[6–8]

Among the two types of capacitor, the charge accumulated in pseudocapacitors is comparatively greater than in the EDLCs. However, the pseudocapacitor electroactive materials suffer from a major problem of shrinking or swelling, which reduces their stable cycling performances. In addition, the larger particle size of the electrode materials can lower the specific capacitance values, as only a smaller surface area is permitted to interact with the electrolyte ions participating in the redox reactions.[9–13] As a result, many researchers have studied various combinations of electroactive materials, like single transition metal oxides/hydroxides (*e.g.* MnO₂, SnO₂, Co₃O₄, Co(OH)₂ and Ni(OH)₂) with carbonaceous substances such as CNT, activated carbon, and graphene, which could help to solve the problems. Also, the active electrode material particle size and morphology are significant in determining the capacitances.

In recent years, alternate electrode materials have been developed that are various combinations of binary and ternary transition metal oxides with different nanoscale morphologies, such as NiMoO₄,[14] CoMoO₄,[15] and MnMoO₄.[16] The formed oxide electrodes with characteristic redox reactions have demonstrated that they exhibit good electrochemical performances. Among the family of metal molybdates, MnMoO₄ has been considered a potential candidate electrode for supercapacitor applications because of the enhanced electrochemical

[a]*Research and Development Centre, Bharathiar University, Coimbatore-641046, India*
[b]*Centre for Advanced Materials Engineering Research and Application, (CAMERA), Department of Chemistry, Rajiv Gandhi College of Engineering and Technology, Kirumampakkam, Puducherry-607403, India. E-mail: dharan9@gmail.com*
[c]*Department of Chemistry, Arignar Anna Government Arts College, Villupuram, 605 602, India*
[d]*Fusion Fuel Cycle Division, Institute for Plasma Research, Gandhinagar, 382010, India*
[e]*Department of Physics, Pondicherry University, Puducherry-605014, India*

properties of the manganese ions.[17] The metal oxide morphologies depend on different synthesis methods. Among them, one-dimensional morphology materials with good physical, chemical and electrochemical properties have been shown to be potential electrodes for supercapacitors. In the literature, there are many reports of one-dimensional nanomaterials synthesised *via* different synthesis routes. Mai *et al.* reported the capacitance of $MnMoO_4/CoMoO_4$ composite nanowires prepared *via* a micro-emulsion method as 187.1 F $g^{-1}$ at 1 A $g^{-1}$.[18] In the reports of Yan *et al.*, the specific capacitance of $MnMoO_4$ nanosheets grown on nickel foam *via* hydrothermal synthesis and annealed in a hydrogen atmosphere to form H–$MnMoO_4$ nanosheets was 376 F $g^{-1}$, which is 17-fold greater than that of the pristine $MnMoO_4$ nanosheets.[19] Ghosh *et al.* reported that $\alpha$-$MnMoO_4$ nanoparticles prepared hydrothermally demonstrated a capacitance of 234 F $g^{-1}$ at 2 A $g^{-1}$.[20] In the reports of Wang *et al.*, 3D fan-like $\alpha$-$MnMoO_4$ nanostructures exhibited a specific capacitance of 562 F $g^{-1}$ at 1 A $g^{-1}$.[21] Senthilkumar *et al.* reported a solution combustion method synthesis of $MnMoO_4$ that gave a specific capacitance of 126 F $g^{-1}$ at a current density of 5 mA $cm^{-2}$.[22] Thus, maintaining the size and morphology of the electrode materials through various synthesis methods has provided a way to enhance the electrochemical properties, conductivity, cyclability and energy and power densities.[23] Recently, a microwave hydrothermal (MH) assisted synthesis method has been extensively used to prepare nanosized sulfides, hydroxides, and oxides with various morphologies. The microwave hydrothermal (MH) method is simple, clean, requires a short time to attain the appropriate reaction temperature, and allows controlled morphology of particles without thermal gradient effects.[24–27]

The present work demonstrates facile synthetic methods for developing pristine $\alpha$-$MnMoO_4$ nanorods *via* co-precipitation (Cp) and microwave hydrothermal (MH) methods. The synthesized $\alpha$-$MnMoO_4$ was characterized using XRD, FTIR, and Raman spectroscopy, and FE-SEM. The electrochemical performances and cycling stability were studied and compared with the literature reports.

# 2. Experiment

## 2.1. Materials and methods

Analytical grade sodium molybdate dihydrate ($Na_2MoO_4 \cdot 2H_2O$), manganese chloride tetrahydrate ($MnCl_2 \cdot 4H_2O$), and sodium hydroxide (NaOH) were purchased from Merck (India). Carbon black, polyvinylidene difluoride (PVdF) and *N*-methyl-2-pyrrolidone (NMP) were purchased from Sigma Aldrich. All chemicals were used as-received without further purification. Nickel foam (1.6 mm thickness) was purchased from MTI Corporation (China). The microwave-assisted synthesis was carried out in a microwave reaction system (SOLV Multiwave PRO, Anton Paar, Germany).

## 2.2. Preparation of Cp-MnMoO₄ nanorods

In a typical procedure, 0.2 mol of $MnCl_2 \cdot 4H_2O$ and 0.2 mol of $Na_2MoO_4 \cdot 2H_2O$ were dissolved in 160 ml of distilled water and thoroughly stirred for 1 h to form a complete precipitate. The addition of 3 M NaOH to the precipitated solution altered the pH to 7 after the solution was continuously stirred for 1 h. The precipitate was filtered and washed three times with distilled water and two times with absolute ethanol. The precipitate $MnMoO_4 \cdot xH_2O$ powder was dried in an oven maintained at 60–70 °C. The powder was calcined at 500 °C for 3 h.

## 2.3. Preparation of MH-MnMoO₄ nanorods

The above-obtained precipitate was transferred into quartz vessels that were positioned on a turntable stage, which rotates the quartz vessels to maintain uniform distribution at 180 °C for 15 min in a microwave reaction system (SOLV, Multiwave PRO Anton-Paar). The program was preset to automatically alter the applied power in order to reach a fixed temperature (180 °C) and a pressure of up to 80 bar. After the completion of the reaction, the quartz vessels in the MW hydrothermal oven were allowed to attain ambient conditions using the inbuilt rapid cooling system. The MW precipitate $MnMoO_4 \cdot xH_2O$ was filtered and washed three times with distilled water and two times with absolute ethanol. Then the obtained $MnMoO_4 \cdot xH_2O$ powders were dried in an oven maintained at 60–70 °C for 12 h. The powder was calcined at 500 °C for 3 h. Henceforth, the co-precipitate and microwave hydrothermal method prepared and heat treated $MnMoO_4$ powders are denoted Cp-$MnMoO_4$ and MH-$MnMoO_4$, respectively.

## 2.4. Material characterization

The prepared powders were characterized using a Powder X-ray diffractometer (X'pert PRO MPD, PANalytical), using Cu-K$\alpha$ radiation ($\lambda = 0.15406$ nm) and an angle 2 theta range from 10° to 80° in steps of 0.02. The average crystallite sizes of the prepared powders were calculated using the Scherrer formula. The structural bonding nature of the thin transparent pellets was recorded using a Thermo Nicolet Fourier Transform Infrared FTIR-6700 spectrometer between 400 and 4000 $cm^{-1}$ for 30 scans. The transparent pellet was made using powders calcined at 500 °C for 3 h and pure KBr crystalline powder, ground in a ratio of 1 : 20. Raman spectra were recorded in the range 100–2000 nm using a Renishaw inVia confocal Raman microscope, UK, with an argon ion laser of 785 nm line, keeping the maximum output power at 100 mW. The morphology and microstructure of the powder calcined at 500 °C for 3 h were identified using a field emission scanning electron microscope (FE-SEM, JSM-6700F, JEOL Ltd).
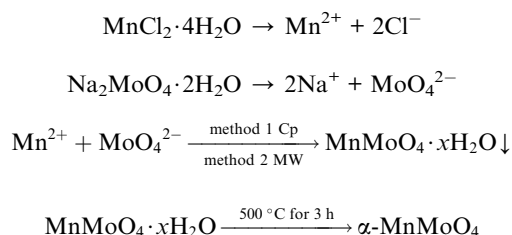
## 2.5. Electrochemical characterization

The working electrode was prepared by mixing the active material $\alpha$-$MnMoO_4$ powder, carbon black as a conducting agent and polyvinylidene difluoride (PVDF) as a binder in a mass ratio of 80 : 10 : 10 to obtain a homogeneous slurry with *N*-methyl pyrrolidone (NMP). For the substrate electrode material prior to coating, several pieces of nickel (Ni) foam were washed with 6 M HCl solution in an ultrasonic bath for 25 min to remove the NiO layer on the surface, and it was cleaned with deionized water followed by absolute ethanol. Then the homogeneous slurry was coated and pressed onto the Ni foam and dried under vacuum at 80 °C for 24 h. A three-electrode cell that

consisted of the working electrode, platinum as the counter electrode and saturated calomel electrode (SCE) as a reference electrode was used, and 2 M sodium hydroxide (2 M NaOH) was used as the electrolyte at room temperature. The electrochemical behavior of the α-MnMoO₄ electrodes was characterized using cyclic voltammetry (CV), galvanostatic charge–discharge, electrochemical impedance spectroscopy (EIS) and cycling stability using a PARSTAT MC Multi-Channel Electrochemical workstation (Ametek, USA). EIS was conducted in the frequency range from $10^4$ to 0.01 Hz with a perturbation amplitude of 10 mV at open circuit potential.

## 3. Results and discussion

### 3.1. Characterization of MnMoO₄

The α-MnMoO₄ powders were prepared *via* co-precipitation (Cp) and microwave hydrothermal methods (MH) using manganese chloride tetrahydrate and sodium molybdate dihydrate as precursors. In both of the preparation methods, the manganese ($Mn^{2+}$) and molybdate ($MoO_4^{2-}$) ions react with each other, resulting in the formation of the $MnMoO_4 \cdot xH_2O$ ceramic. Finally, $MnMoO_4 \cdot xH_2O$ was calcined at 500 °C for 3 h to attain the phase pure α-MnMoO₄ rod like nanocrystalline ceramics. The overall reaction is represented as follows:

$$MnCl_2 \cdot 4H_2O \rightarrow Mn^{2+} + 2Cl^-$$

$$Na_2MoO_4 \cdot 2H_2O \rightarrow 2Na^+ + MoO_4^{2-}$$

$$Mn^{2+} + MoO_4^{2-} \xrightarrow[\text{method 2 MW}]{\text{method 1 Cp}} MnMoO_4 \cdot xH_2O \downarrow$$

$$MnMoO_4 \cdot xH_2O \xrightarrow{500\,°C\ for\ 3\ h} \alpha\text{-}MnMoO_4$$

The XRD patterns of the as-prepared MH-MnMoO₄ dried at 60 °C, and the Cp-MnMoO₄ and MH-MnMoO₄ powders heat treated at 500 °C, are shown in Fig. 1. In Fig. 1(a), the characteristic peaks of hydrated $MnMoO_4 \cdot 4H_2O$ are observed, which indicates that further calcination is required to dehydrate the MnMoO₄ powder. The XRD pattern is well in agreement with the standard diffraction pattern of $MnMoO_4 \cdot 4H_2O$ (JCPDS no. 01-078-0220).[20] In Fig. 1(b and c), the XRD patterns of the Cp-MnMoO₄ and MH-MnMoO₄ powders heat treated at 500 °C for 3 h showed that peaks appear at 25.2, 31.2, 32.4, 38.5, 44.7 and 52.4, which are assigned to (220), (112), (022), (113), (225) and (440) planes, respectively. The diffraction peaks are well in agreement with the standard monoclinic phase α-MnMoO₄ (JCPDS card no. 01-072-0285). Moreover, the presence of the major (220) reflection in the XRD spectra indicates the presence of the α-phase.[19,28] The crystallite sizes of the Cp-MnMoO₄ and

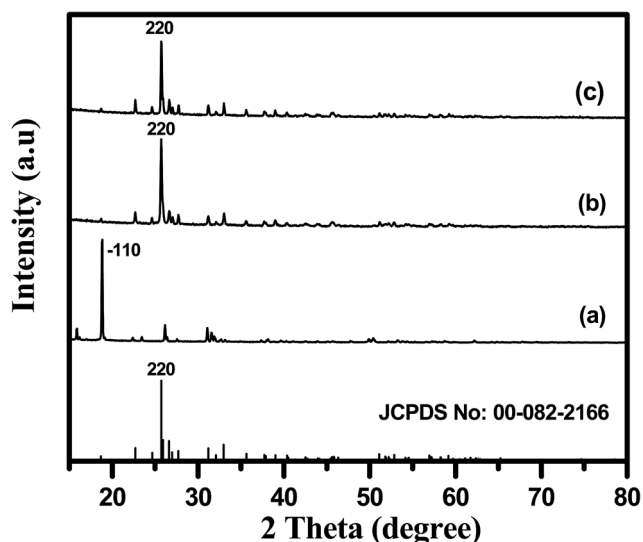Fig. 2 FTIR spectra of the (a) Cp-MnMoO₄ and (b) MH-MnMoO₄ powders calcined at 500 °C for 3 h.

Fig. 1 XRD patterns of (a) as-prepared MH-MnMoO₄ and (b and c) MH-MnMoO₄ and Cp-MnMoO₄ samples calcined at 500 °C for 3 h.

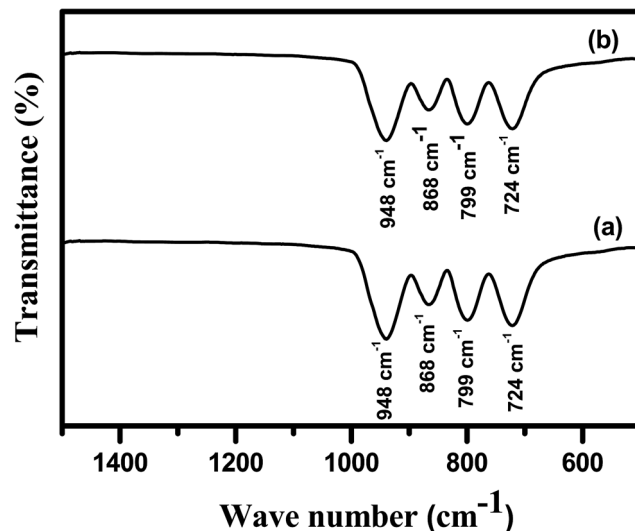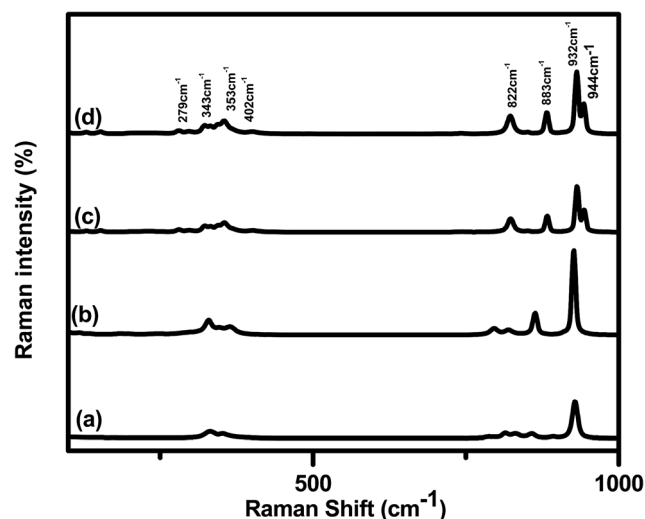Fig. 3 Raman spectra of (a) the as-prepared Cp-MnMoO₄ (b) and the as-prepared MH-MnMoO₄, and (c and d) the Cp-MnMoO₄ and MH-MnMoO₄ samples calcined at 500 °C for 3 h.
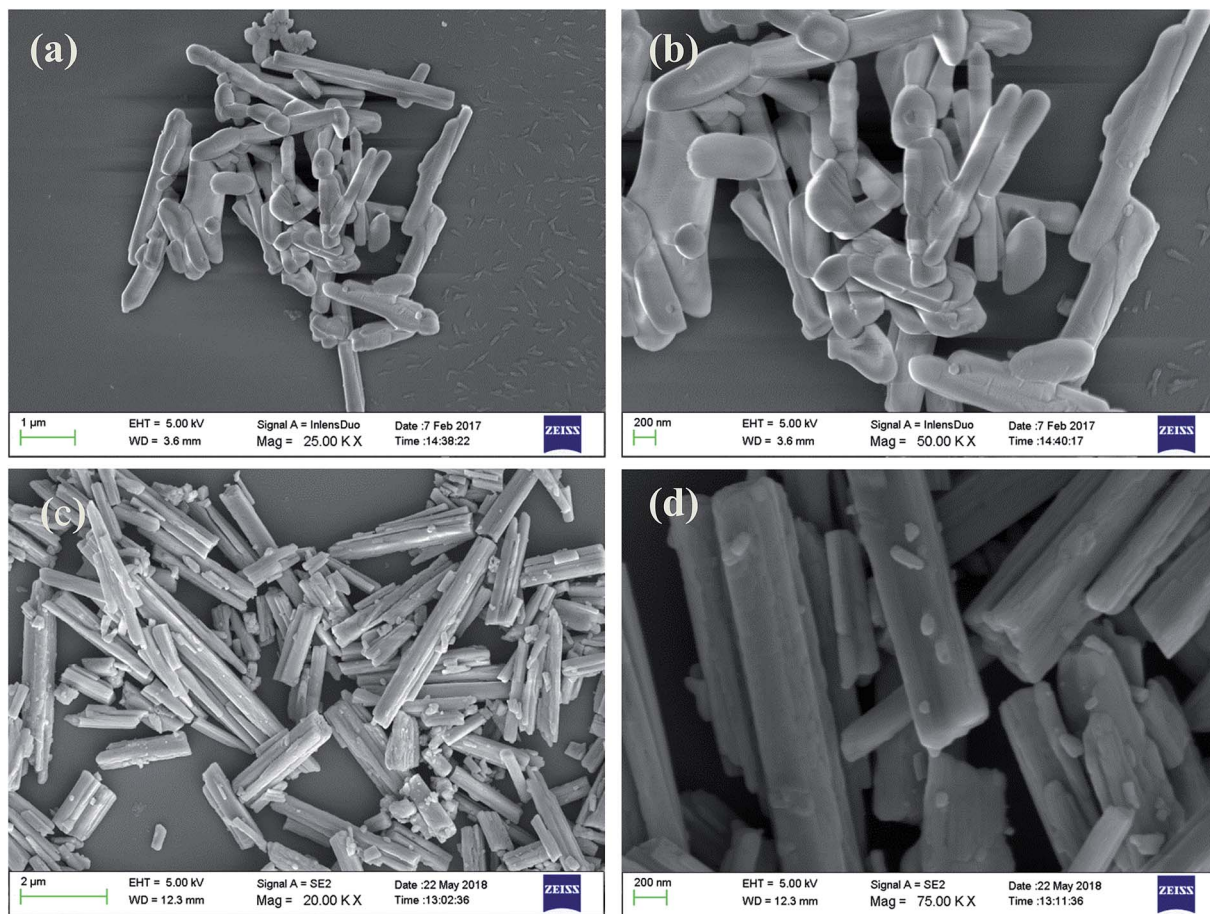
**Fig. 4** FE-SEM images of (a and b) Cp-MnMoO₄ and (c and d) MH-MnMoO₄ powders calcined at 500 °C for 3 h.

MH-MnMoO₄ powders were calculated using the Scherrer equation: $t = 0.9\lambda/\beta\cos\theta$, where $t$ is the average crystallite size, $\lambda$ is the wavelength of the incident X-rays of Cu-K$\alpha$ radiation, $\beta$ is the full width half maxima of the diffraction peak and $\theta$ is the Bragg diffraction angle.[29] The crystallite sizes of Cp-MnMoO₄ and MH-MnMoO₄ are found to be 43 nm and 26 nm, respectively.

The FTIR spectra of Cp-MnMoO₄ and MH-MnMoO₄ powders calcined at 500 °C for 3 h are shown in Fig. 2(a and b), respectively. From Fig. 2(a and b), it is observed that the synthesized α-MnMoO₄ showed four strong FTIR bands at 724, 799, 868 and 948 cm⁻¹. The 948 cm⁻¹ strong band corresponds to the stretching vibration of the Mo=O group. The 868 cm⁻¹ band is attributed to the bending vibration of the Mo–O–Mo group. The bands at 724 and 799 are characteristic bands of the Mo–O stretching vibration in the tetrahedral MoO₄ groups.[30–32] The presence of the strong bands confirms the formation of tetrahedrally coordinated Mo on the surface of α-MnMoO₄.

The Raman spectra of the Cp-MnMoO₄ and MH-MnMoO₄ powders, each as-prepared and each calcined at 500 °C for 3 h, are shown in Fig. 3(a, b, c and d), respectively. From Fig. 3(a and b), it is observed that the as-prepared Cp-MnMoO₄ and MH-MnMoO₄ powders exhibit a high intensity band at 926 cm⁻¹, moderate intensity bands at 862 cm⁻¹ and 328 cm⁻¹, and low
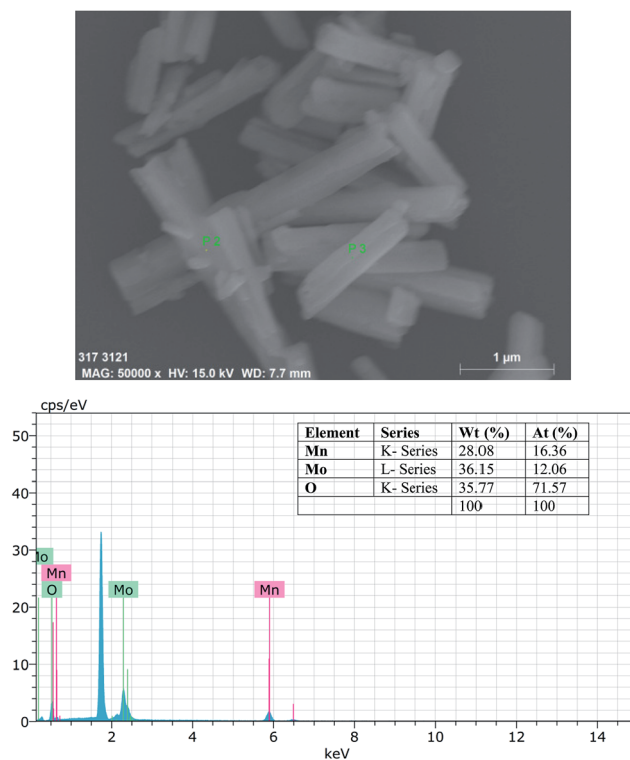


| Element | Series | Wt (%) | At (%) |
|---------|--------|--------|--------|
| Mn | K- Series | 28.08 | 16.36 |
| Mo | L- Series | 36.15 | 12.06 |
| O | K- Series | 35.77 | 71.57 |
| | | 100 | 100 |

**Fig. 5** EDS spectra of MH-MnMoO₄ powders calcined at 500 °C for 3 h.
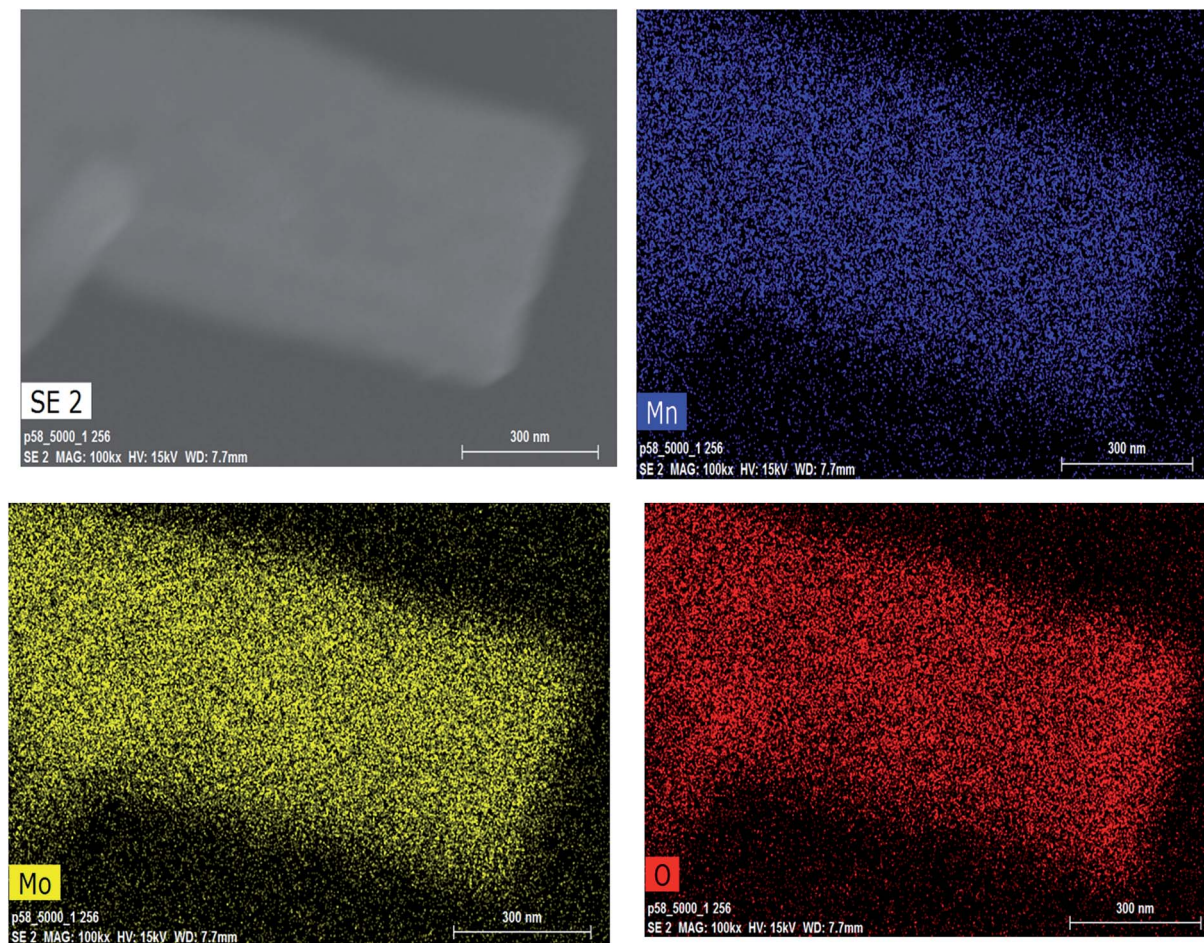
Fig. 6    SEM-EDS elemental mapping of Mn, Mo and O for MH-MnMoO$_4$ powders calcined at 500 °C for 3 h.

intensity bands at 820 cm$^{-1}$, 796 cm$^{-1}$ and 363 cm$^{-1}$, which are the characteristic bands of MnMoO$_4\cdot$H$_2$O.[20] In accordance with group theory, the $\alpha$-MnMoO$_4$ ceramic has 13 Raman active modes of vibration (3A$_g$ + 5B$_g$ + 5E$_g$). From Fig. 3(c and d), it is observed that the calcined Cp-MnMoO$_4$ and MH-MnMoO$_4$ powders show that the bands at 944, 932 and 822 cm$^{-1}$ are assigned to the A$_g$ mode, and the bands at 883 and 343 cm$^{-1}$ are assigned to the B$_g$ (+A$_g$) and A$_g$ (+B$_g$) modes. The band present at 402 cm$^{-1}$ is assigned to the B$_g$ mode and the bands at 372 and 279 cm$^{-1}$ are assigned to the A$^b_g$ (B$_g$) modes. The highly intense bands at 933 and 822 cm$^{-1}$ are due to M(1)O(2) and M(1)O(1) symmetric stretching vibrations, respectively, and the assigned modes are in accordance with the reported data.[28]

Field-emission scanning electron microscope (FE-SEM) images of the Cp-MnMoO$_4$ and MH-MnMoO$_4$ powders are shown in Fig. 4. From Fig. 4(a and b), it is observed that the FE-SEM images of Cp-MnMoO$_4$ reveal a smooth surface nanorod morphology, and that the nanorods are ∼200 nm in diameter and ∼1.6 μm in length. From Fig. 4(c and d), it is observed that the FE-SEM images of MH-MnMoO$_4$ reveal that five to six nanorods of diameter 100–150 nm aligned to form tube-like morphology and the tube-like structure is about ∼600 nm in diameter and ∼1.6 μm in length. In order to study the chemical

composition, elemental analysis was performed using energy-dispersive spectrometry (EDS). The EDS spectra showed the presence of Mn, Mo and O. The atomic percentage composition of Mn, Mo and O of the nanorods clearly confirmed that the Mn, Mo and O atomic ratio of 1 : 1 : 4 was present in the aggregated nanorods forming the tube-like morphology, as shown in Fig. 5. Furthermore, to study the elemental distribution of the MH-MnMoO$_4$ sample, elemental mapping was carried out and the mapping of the surface showed a uniform distribution of Mn, Mo and O, as shown in Fig. 6. The uniform distribution of these elements would most likely facilitate the formation of pure MnMoO$_4$. The aggregated nanorods forming a tube-like morphology make an easy path for the transport of ions, resulting in enhanced electrochemical performance.

### 3.2.   Electrochemical studies

The cyclic voltammetric (CV) curves of the Cp-MnMoO$_4$ and MH-MnMoO$_4$ nanorod electrodes at various scan rates from 10 to 100 mV s$^{-1}$ using 2 M NaOH as the electrolyte in the potential range of 0–0.6 V are shown in Fig. 7(a and b). In Fig. 7(a and b), the CV curves show the presence of a redox peak, which is attributed to the transition of Mn$^{(2+)}$/Mn$^{(3+)}$.[18] The anodic peak at around 0.3 V corresponds to the oxidation process of Mn$^{2+}$ to
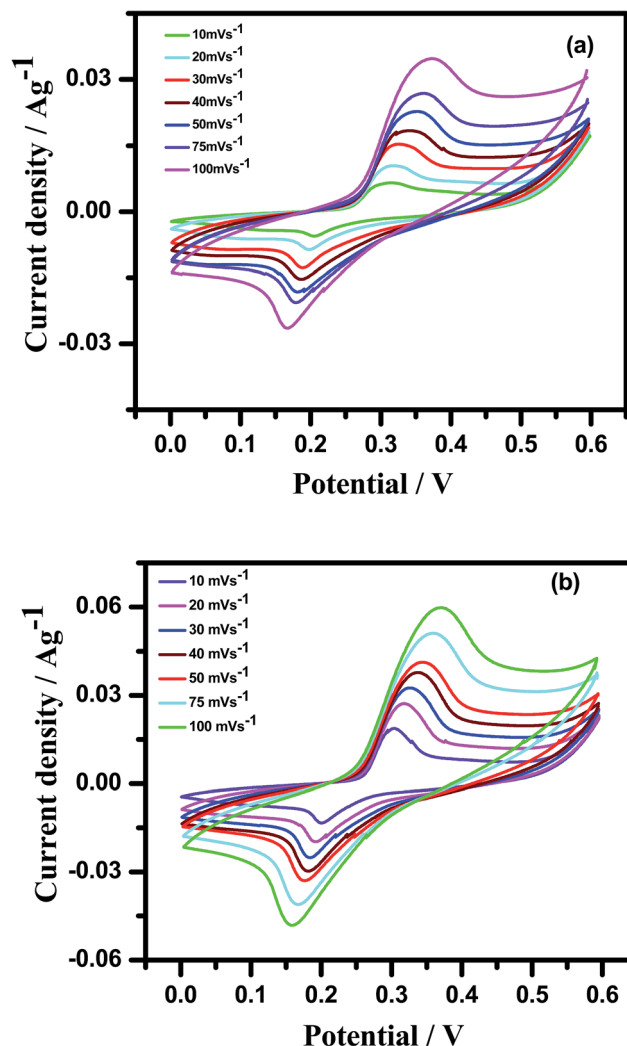
**Fig. 7** Cyclic voltammetric curves of (a) Cp-MnMoO$_4$ and (b) MH-MnMoO$_4$ in 2 M NaOH electrolyte at different scan rates.
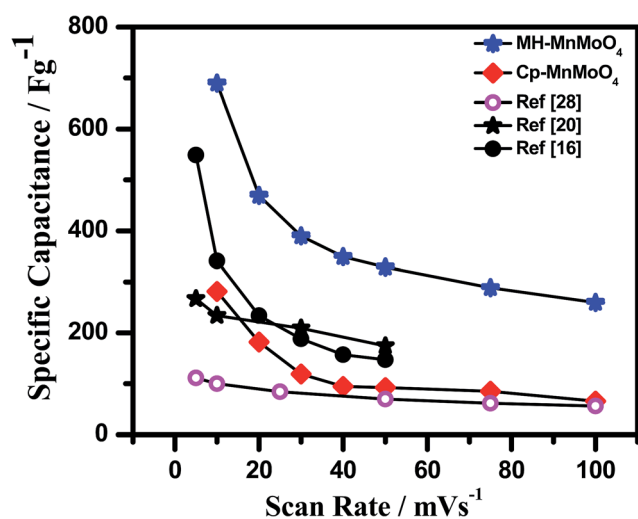
Mn$^{3+}$. The cathodic peak at around 0.15 V refers to the reduction process of Mn$^{3+}$ to Mn$^{2+}$. At different scan rates, 10–100 mV s$^{-1}$, the shapes of the CV curves do not change, but the CV curve peak positions widely shift. The anodic peaks gradually move to higher potentials, whereas the cathodic peaks shift to lower potentials in the opposite direction. As a result, it is identified that at higher scan rates, the electronic and ionic movements are rapid and a fast redox reaction occurs at the interface of electroactive material/electrolyte.[33,34] In addition, during the CV analysis, molybdate (Mo) ions do not participate in the redox process, but they promote the electrical conductivity at ambient temperature.[18] Using the CV data and galvanostatic charge/discharge data in eqn (1) and (2), respectively, the specific capacitances are calculated for the Cp-MnMoO$_4$ and MH-MnMoO$_4$ nanorod electrodes.

$$C_s = \frac{Q}{\Delta V m} \ \text{F g}^{-1} \tag{1}$$





**Fig. 8** Comparison of specific capacitances of Cp-MnMoO$_4$ and MH-MnMoO$_4$ calculated from CV curves with other reported results.
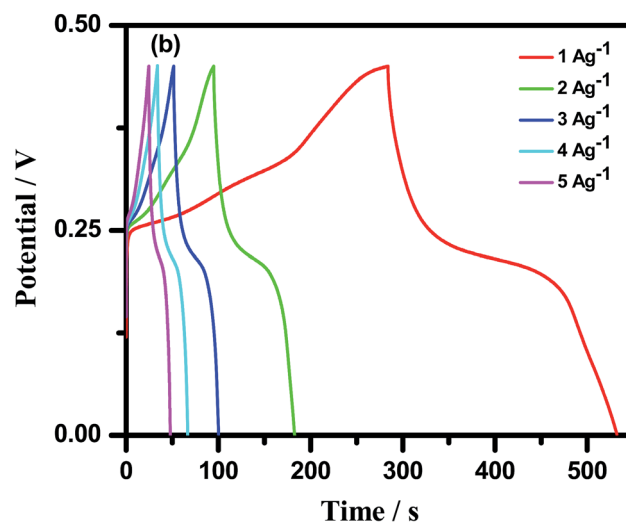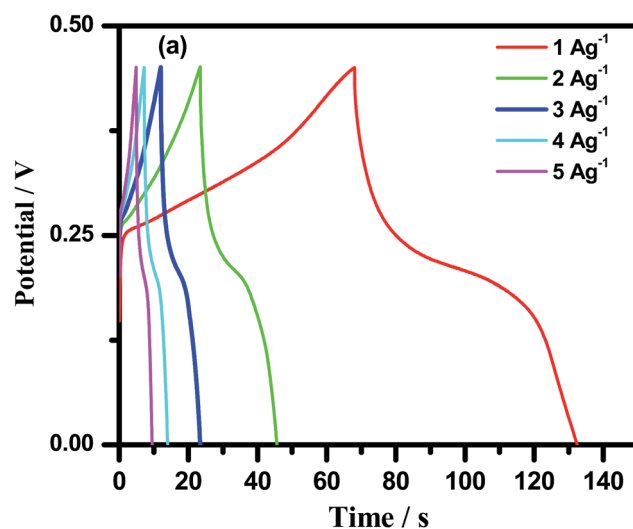
**Fig. 9** Galvanostatic charge–discharge curves of (a) Cp-MnMoO$_4$ and (b) MH-MnMoO$_4$ with different discharge current densities in 2 M NaOH.
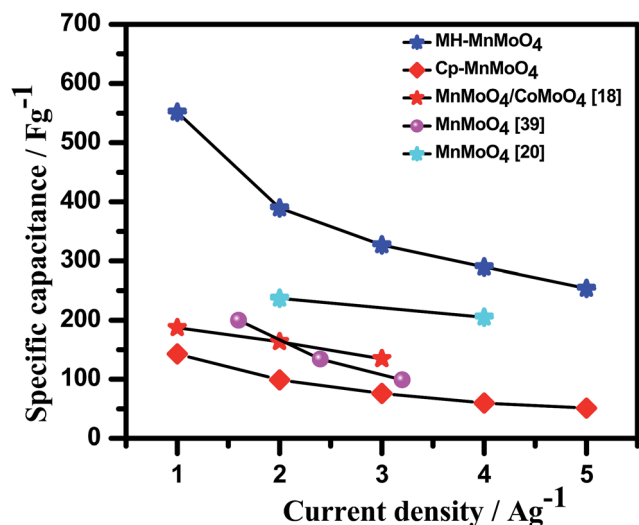
Fig. 10 Comparison of the specific capacitances of Cp-MnMoO$_4$ and MH-MnMoO$_4$ calculated from GCD analysis with the literature reports.

$$C_s = \frac{I\Delta t}{m\Delta V} \ \text{F g}^{-1} \qquad (2)$$

where $C_s$ is the specific capacitance, $Q$ is the average charge of the electrode (Coulomb), $\Delta V$ is the potential window, $m$ (g) is the loaded mass of the active material, $I$ (A) is the discharge current and $\Delta t$ (s) is the discharge time.[35,36]

The Cp-MnMoO$_4$ and MH-MnMoO$_4$ nanorod electrodes demonstrated that the specific capacitance decreases as the scan rate increases, which is consistent with the literature reports, as shown in Fig. 8. The calculated $C_s$ values for the Cp-MnMoO$_4$ nanorods are 281, 181, 119, 94, 92, 85, and 65 F g$^{-1}$ at scan rates of 10, 20, 30, 40, 50, 75 and 100 mV s$^{-1}$, respectively. On the other hand, the MH-MnMoO$_4$ nanorod electrodes reveal significantly enhanced $C_s$ values of 689, 469, 389, 349, 328, 228 and 259 F g$^{-1}$ at scan rates of 10, 20, 30, 40, 50, 75 and 100 mV s$^{-1}$, respectively. From Fig. 8, it is observed that the calculated specific capacitance decreases from 281 to 65 F g$^{-1}$ and 689 to

259 F g$^{-1}$ as the scan rate increases for the Cp-MnMoO$_4$ and MH-MnMoO$_4$ nanorod electrodes. The decrease in $C_s$ may be due to the faster mobility of the electrolyte ions at higher scan rates, and as a result the ions are not able to utilize the active material completely.[37] Moreover, the nanorods prepared via the MH method show a significantly higher $C_s$, which may be due to their aspect ratio and the easy interaction mobility of the electrolyte ions. From Fig. 8, it is observed that the literature report samples have lower specific capacitances than the samples in the present work prepared via the MH method, which showed higher specific capacitances.

The galvanostatic charge–discharge curves at different current densities with a potential window between 0 and 0.45 V for Cp-MnMoO$_4$ and MH-MnMoO$_4$ nanorod electrodes are shown in Fig. 9(a and b). From Fig. 9(a and b), it is observed that the quasi-symmetric charge–discharge profile suggests that the pseudocapacitive behavior of the material and the specific capacitances were calculated using eqn (2). Fig. 10 shows the decrease in specific capacitance values of 142, 99, 76, 59 and 51 F g$^{-1}$ with respect to the different discharge current densities of 1, 2, 3, 4, and 5 A g$^{-1}$, respectively, for Cp-MnMoO$_4$. On the other hand, the powder prepared via the MH method, resulting in fine nanorods, demonstrates specific capacitance values of 551, 389, 326, 289, and 253 F g$^{-1}$ at the current densities of 1, 2, 3, 4 and 5 A g$^{-1}$, respectively, which are higher than the those in the compared literature reports.[18,39,40] From Fig. 10, it is observed that an increase in the current density decreases the capacitance value, which may be because of a decrease in the diffusion ions in the inner active sites of the electrode material.[38] The increase in the specific capacitance value of 551 F g$^{-1}$ at a current density of 1 A g$^{-1}$ may be because of the one-dimensional morphological structure. The well-defined nanorods enable the surface of the nanorods to be effectively accessible to the electrolyte and allow faster mobility of the electrons in the electrode. As a result, an improved high specific capacitance and enhanced electrochemical kinetics at high current densities are obtained for the nanorods. From Fig. 10, it is observed that the present MnMoO$_4$ prepared via the MH method showed higher specific capacitance than that of the

Table 1 Comparison of the specific capacitances of Cp-MnMoO$_4$ and MH-MnMoO$_4$ nanorod electrodes with the literature reports for supercapacitor applications

| S. no. | Material | Method | Specific capacitance (F g$^{-1}$) | Scan rate mV s$^{-1}$ (or) current density (A g$^{-1}$) | Ref. |
|---|---|---|---|---|---|
| 1 | MnMoO$_4$ | Co-precipitation | 281 F g$^{-1}$, 142 F g$^{-1}$ | 10 mV s$^{-1}$, 1 A g$^{-1}$ | Present work |
| 2 | MnMoO$_4$ | Microwave hydrothermal method | 689 F g$^{-1}$, 551 F g$^{-1}$ | 10 mV s$^{-1}$, 1 A g$^{-1}$ | Present work |
| 3 | MnMoO$_4$ | Precipitation technique | 200 F g$^{-1}$ | 1.6 A g$^{-1}$ | 39 |
| 4 | MnMoO$_4$/graphene | Hydrothermal method | 364 F g$^{-1}$ | 2 A g$^{-1}$ | 20 |
| 5 | MnMoO$_4$ MnMoO$_4$/CoMoO$_4$ | Micro-emulsion method | 9.7 F g$^{-1}$, 187 F g$^{-1}$ | 1 A g$^{-1}$, 1 A g$^{-1}$ | 18 |
| 6 | MnMoO$_4$ nanoparticles MnMoO$_4$ nanorods | Simple method | 371 F g$^{-1}$, 469 F g$^{-1}$ | 1 A g$^{-1}$, 1 A g$^{-1}$ | 21 |
| 7 | MnMoO$_4$/PPy | In situ oxidative polymerization | 462.9 F g$^{-1}$, 374.8 F g$^{-1}$ | 5 mV s$^{-1}$, 0.2 A g$^{-1}$ | 40 |
| 8 | MnMoO$_4$ | Hydrothermal method | 234 F g$^{-1}$ | 10 mV s$^{-1}$ | 18 |
| 9 | Amorphized MnMoO$_4$ | Hydrothermal method | 373 F g$^{-1}$ | 5 mV s$^{-1}$ | 25 |
| 10 | MnMoO$_4$·H$_2$O | Hydrothermal method | 549 F g$^{-1}$ | 5 mV s$^{-1}$ | 19 |
| 11 | MnMoO$_4$/polyaniline | In situ oxidative polymerization | 396 F g$^{-1}$ | 5 mV s$^{-1}$ | 23 |
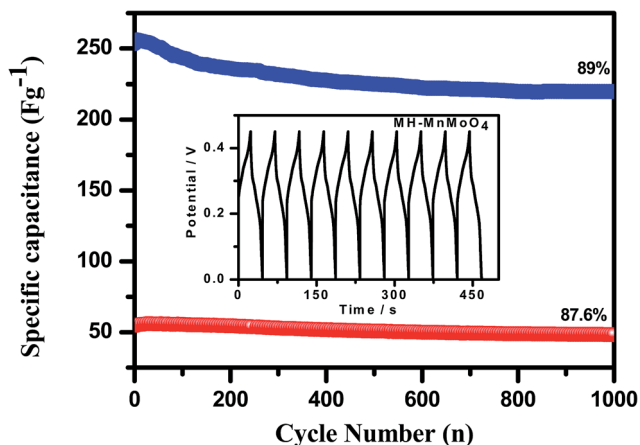
Fig. 11 Cycling performance of the Cp-MnMoO$_4$ and MH-MnMoO$_4$ electrodes at a current density of 5 A g$^{-1}$ (the inset figure shows the first ten galvanostatic charge−discharge profiles of the MH-MnMoO$_4$ electrode at 5 A g$^{-1}$).

observed that about 89% of the initial capacitance was retained even after 1000 cycles at a high current density, which demonstrates the good cycling stability of the MH-MnMoO$_4$ nanorods that aggregated to form a tube-like morphology electrode at a high current density. A small increase in the charge transfer resistance that is observed for the Cp-MnMoO$_4$ electrode reveals 87.6% capacitance retention after 1000 cycles.

The galvanostatic charge–discharge measurements were carried out at different current densities of 1, 2, 3, 4 and 5 A g$^{-1}$ for 100 cycles, as shown in Fig. 12. From Fig. 12 it is observed that the MH-MnMoO$_4$ nanorods that aggregated to form a tube-like morphology electrode material exhibit high reversible capacity, high capacitance retention performance and excellent cycling stability as the cycling current varies from low (1 A g$^{-1}$) to high (5 A g$^{-1}$) current with changes every 10 cycles, and reverses back to a low current of 1 A g$^{-1}$. Thus, the high rate performance and good reversible capacity retention at different

MnMoO$_4$ samples reported in the literature. Table 1 compares the specific capacitances measured at different scan rates and current densities for the MnMoO$_4$ electrodes prepared *via* various synthesis methods. From Table 1, it is noted that the MH-MnMoO$_4$ electrode shows high specific capacitance as compared with the electrodes from the literature reports, such as MnMoO$_4$ (200 F g$^{-1}$ at 1.6 A g$^{-1}$),[39] the MnMoO$_4$ (9.7 F g$^{-1}$ at 1 A g$^{-1}$) and MnMoO$_4$/CoMoO$_4$ nanocomposite (187.1 F g$^{-1}$ at 1 A g$^{-1}$),[18] and the MnMoO$_4$/PPy nanocomposite (462.9 F g$^{-1}$ at 5 mV s$^{-1}$).[40]

The cycling stability study of the Cp-MnMoO$_4$ and MH-MnMoO$_4$ nanorod electrodes was carried out using galvanostatic charge–discharge measurements at a constant current density of 5 A g$^{-1}$ for 1000 cycles. The specific capacitance and the capacitance retention with respect to the number of cycles are shown in Fig. 11, and the inset figure shows the first ten charge–discharge cycles of MH-MnMoO$_4$. From Fig. 11, it is
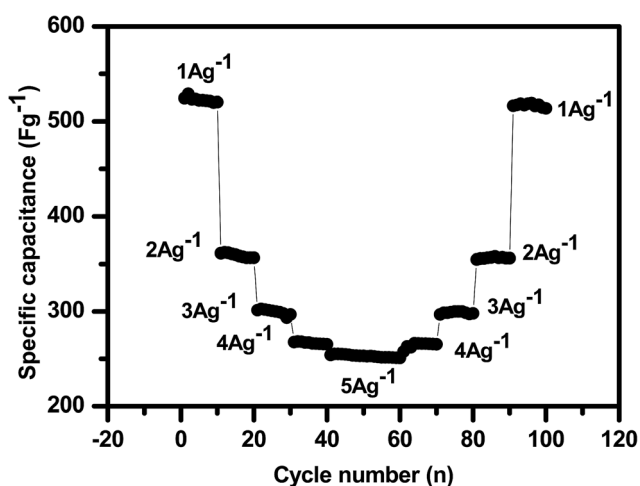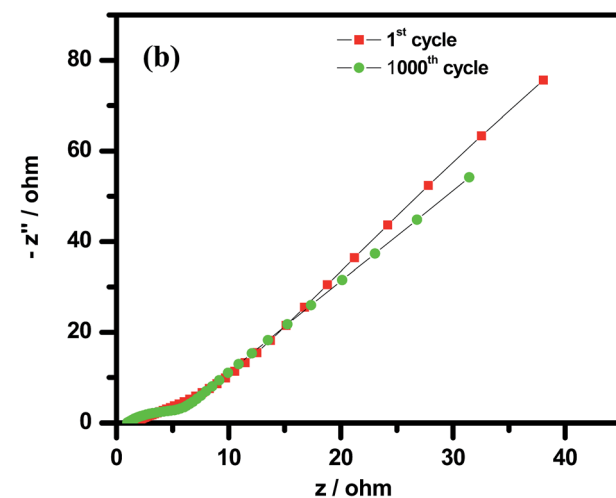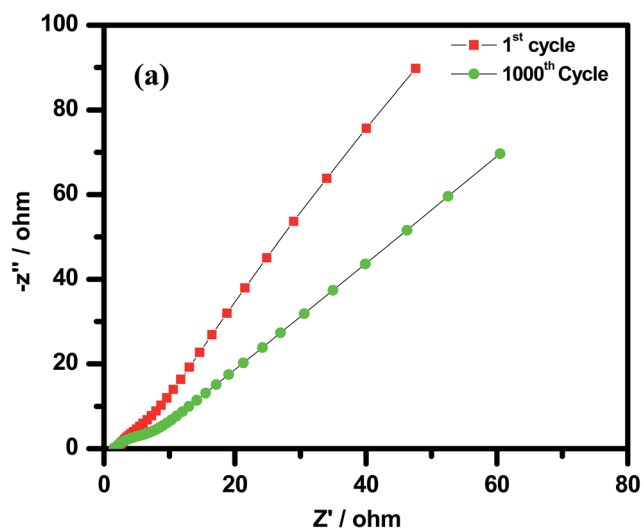


Fig. 12 Cycling stability test of the MH-MnMoO$_4$ electrode at various current densities for 100 cycles.



Fig. 13 Electrochemical impedance spectra of the (a) Cp-MnMoO$_4$ and (b) MH-MnMoO$_4$ electrodes after the 1$^{st}$ and 1000$^{th}$ galvanostatic charge−discharge cycles at a current density of 5 A g$^{-1}$.

current densities demonstrate the structural stability of the calcined MH-MnMoO$_4$ nanorods, which are capable of delivering the required high energy at various load levels and are confirmed to be a promising electrode material for supercapacitor applications.[41]

Electrochemical impedance spectroscopy (EIS) of the Cp-MnMoO$_4$ and MH-MnMoO$_4$ electrodes was performed at open circuit potential with a frequency range from 10 kHz to 0.01 Hz after the 1$^{st}$ and 1000$^{th}$ cycles at a current density of 5 A g$^{-1}$. The EIS spectra of the Cp-MnMoO$_4$ and MH-MnMoO$_4$ electrodes after the 1$^{st}$ and 1000$^{th}$ cycle are shown in Fig. 13(a and b). From Fig. 13(a and b), the presence of a semi-circle at the higher frequency range is observed, which is due to the capacitance in parallel with the ionic charge transfer resistance. The presence of a linear part in the low-frequency region, called the Warburg resistance ($Z_w$), is also observed, which is due to the frequency dependent ion diffusion or transport in the electrolyte to the electrode surface.[36] From Fig. 13(a and b), it is noted that the slight increase in the radius of the depressed semi-circle in the high-frequency region after the 1000$^{th}$ cycle compared to the 1$^{st}$ cycle reveals the small decrease in the interfacial charge transfer conductivity of the Cp-MnMoO$_4$ and MH-MnMoO$_4$ electrodes. In the low-frequency region, the Warburg resistance slightly increased after 1000 cycles and the slope was not altered, which suggests that the mobility of the ions from the electrolyte to the electrode surface was not relatively altered. The internal drop in the specific capacitance can be attributed to the slight decrease in the interfacial charge transfer conductivity, which causes a decrease in the retention from the initial capacitance for Cp-MnMoO$_4$ (87.6%) and MH-MnMoO$_4$ (89%) during the cycling performance.

The variation of energy density as a function of power density for the Cp-MnMoO$_4$ and MH-MnMoO$_4$ electrodes is shown in Fig. 14. The energy density and power density were derived from the charge/discharge curves at various current densities and these can be calculated from the following equations.[34]
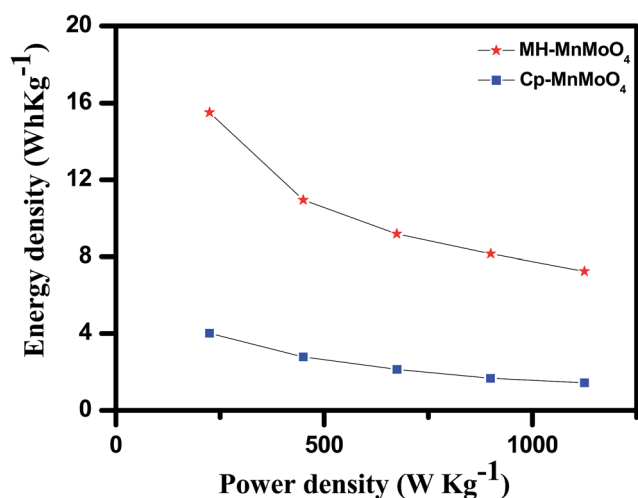
$$E = \frac{1}{2}C_s(\Delta V)^2 \ \text{W h kg}^{-1} \quad (3)$$

$$P = \frac{Q\Delta V}{2T} = \frac{E}{T} \ \text{W kg}^{-1} \quad (4)$$

where $P$ is the power density (W kg$^{-1}$), $E$ is the energy density (W h kg$^{-1}$), $C_s$ is the specific capacitance based on the mass of the electroactive material (F g$^{-1}$), $Q$ is the total charge delivered (C), $\Delta V$ is the potential window of discharge (V), and $T$ is the discharge time (s). From Fig. 14, it is observed that the energy density decreases with an increase in power density. The maximum energy density obtained for the Cp-MnMoO$_4$ and MH-MnMoO$_4$ electrodes is 4.01 and 15.5 W h kg$^{-1}$ at the power density of 224.8 and 224.9 W kg$^{-1}$, respectively. The high energy density without any significant loss of power density demonstrated that the MH-MnMoO$_4$ nanorods that aggregated to form a tube-like morphology electrode could vitally be considered as an efficient supercapacitor electrode material.

## 4. Conclusion

One dimensional α-MnMoO$_4$ nanorods have been successfully synthesized via co-precipitation, and the nanorods aggregated to form a tube-like morphology via a microwave hydrothermal method. The MH-MnMoO$_4$ electrode exhibited a maximum specific capacitance value of 551 F g$^{-1}$ at a current density of 1 A g$^{-1}$, compared with the Cp-MnMoO$_4$ nanorod electrode. The cycling stability revealed a good reversibility with a cycling efficiency of 89% after 1000 cycles at 5 A g$^{-1}$. The high rate performances and good reversible capacity retention at different current densities demonstrated the structural stability of the calcined MH-MnMoO$_4$. Thus, the facile microwave hydrothermal approach to synthesise α-MnMoO$_4$ nanorods that aggregated to form a tube-like morphology is a valuable method to obtain promising electrodes with high energy density and without significant loss of power density for high electrochemical performance supercapacitors.

## Conflicts of interest

There are no conflicts to declare.

## Acknowledgements

## References

1 X. Peng, L. Peng, C. Wu and Y. Xie, *Chem. Soc. Rev.*, 2014, **43**, 3303.
2 Y. Shao, M. F. El-Kady, L. J. Wang, Q. Zhang, Y. Li, H. Wang, M. F. Mousavi and R. B. Kaner, *Chem. Soc. Rev.*, 2015, **44**, 3639.



Fig. 14 Ragone plots (power density vs. energy density) of the Cp-MnMoO$_4$ and MH-MnMoO$_4$ electrodes.

3 H. Wang, Y. Yang, Y. Liang, J. T. Robinson, Y. Li, A. Jackson, Y. Cui and H. Dai, *Nano Lett.*, 2011, **11**, 2644.

4 Q. Zhang, Y. Deng, Z. Hu, Y. Liu, M. Yao and P. Liu, *Phys. Chem. Chem. Phys.*, 2014, **16**, 23451.

5 D. S. Patil, J. S. Shaikh, D. S. Dalavi, S. S. Kalagi and P. S. Patil, *Mater. Chem. Phys.*, 2011, **128**, 449.

6 K. Chen and D. Xue, *Chem. Rec.*, 2018, **18**, 282.

7 K. Chen and D. Xue, *Nanotechnology*, 2018, **29**, 024003.

8 K. Chen, F. Liu, X. Liang and D. Xue, *Surf. Rev. Lett.*, 2017, **24**(03), 1730005.

9 K. Chen and D. Xue, *Mater. Res. Bull.*, 2017, **96**, 281.

10 K. Chen and D. Xue, *Mater. Res. Bull.*, 2016, **83**, 201.

11 K. Chen, G. Li and D. Xue, *Funct. Mater. Lett.*, 2016, **9**, 1640001.

12 K. Chen and D. Xue, *Sci. China: Technol. Sci.*, 2015, **58**, 1768.

13 K. Chen, S. Song, F. Liu and D. Xue, *Chem. Soc. Rev.*, 2015, **44**, 6230.

14 Z. Yin, S. Zhang, Y. Chen, P. Gao, C. Zhu, P. Yang and L. Qia, *J. Mater. Chem. A*, 2015, **3**(2015), 739.

15 G. K. Veerasubramani, K. Krishnamoorthy and S. J. Kim, *RSC Adv.*, 2015, **5**, 16319.

16 Y. Cao, W. Li, K. Xu, Y. Zhang, T. Ji, R. Zou, J. Yang, Z. Qin and J. Hu, *J. Mater. Chem. A*, 2014, **2**, 20723.

17 S. S. Kim, S. Ogura, H. Ikuta, Y. Uchimoto and M. Wakihara, *Chem. Lett.*, 2001, **8**, 760.

18 L. Q. Mai, F. Yang, Y. L. Zhao, X. Xu, L. Xu and Y. Z. Luo, *Nat. Commun.*, 2011, **2**, 381.

19 X. Yan, L. Tian, J. Murowchick and X. Chen, *J. Mater. Chem. A*, 2016, **4**, 3683.

20 D. Ghosh, S. Giri, Md. Moniruzzaman, T. Basu, M. Mandala and C. K. Das, *Dalton Trans.*, 2014, **43**, 11067.

21 L. Wang, L. Yue, X. Zang, H. Zhu, X. Hao, Z. Leng, X. Liu and S. Chen, *CrystEngComm*, 2016, **18**, 9286.

22 B. Senthilkumar, K. Vijaya Sankar, R. Kalai Selvan, M. Danielle and M. Manickam, *RSC Adv.*, 2013, **3**, 352.

23 J. Yesuraj, V. Elumalai, M. Bhagavathiachari, A. S. Samuel, E. Elaiyappillai and P. M. Johnson, *J. Electroanal. Chem.*, 2017, **797**, 78.

24 K. Chen, Y. D. Noh, R. R. Patel and D. Xue, *Ceram. Int.*, 2014, **40**, 8183.

25 K. Chen, Y. D. Noh, W. Huang and D. Xue, *Ceram. Int.*, 2014, **40**, 2877.

26 K. Chen, Y. D. Noh, A. C. Donahoe and D. Xue, *Ceram. Int.*, 2014, **40**, 3155.

27 K. Chen, Y. D. Noh, K. Li, S. Komarneni and D. Xue, *J. Phys. Chem. C*, 2013, **117**, 10770.

28 G. Veerasubramani, K. Krishnamoorthy, R. Sivaprakasam and S. J. Kim, *Mater. Chem. Phys.*, 2014, **147**, 836.

29 A. Mirmohsenia, M. S. Seyed Dorrajia and M. G. Hosseinib, *Electrochim. Acta*, 2012, **70**, 182.

30 S. J. Lei, K. B. Tang, Q. C. Liu, Z. Fang, Q. Yang and H. G. Zheng, *J. Mater. Sci.*, 2006, **41**, 473.

31 T. S. Sian and G. B. Reddy, *Appl. Surf. Sci.*, 2004, **236**, 1.

32 L. Seguin, M. Figlarz, R. Cavagnat and J.-C. Lasskgues, *Spectrochim. Acta, Part A*, 1995, **51**, 1323.

33 D. Cai, B. Liu, D. Wang, Y. Liu, L. Wang, H. Li, Y. Wang, C. Wang, Q. Li and T. Wang, *Electrochim. Acta*, 2014, **125**, 294.

34 I. Shakir, M. Shahid, H. W. Yang and D. J. Kang, *Electrochim. Acta*, 2010, **56**, 376.

35 P. Vinothbabu and P. Elumalai, *RSC Adv.*, 2014, **4**, 31219.

36 K. Liu, Z. Hu, R. Xue, J. Zhang and J. Zhu, *J. Power Sources*, 2008, **179**, 858.

37 S. Saranya, R. K. Selvan and N. Priyadharsini, *Appl. Surf. Sci.*, 2012, **258**, 4881.

38 P. Justin and G. R. Rao, *Int. J. Hydrogen Energy*, 2010, **35**, 9709.

39 B. Senthilkumar, R. Kalai Selvan, D. Meyrick and M. Minakshi, *Int. J. Electrochem. Sci.*, 2015, **10**, 185.

40 H. Wang, Y. Song, J. Zhou, X. Xu, W. Hong, J. Yan, R. Xue, H. Zhao, Y. Liu and J. Gao, *Electrochim. Acta*, 2016, **212**, 775.

41 S. Devaraj, H. Y. Liu and P. Balaya, *J. Mater. Chem. A*, 2014, **2**, 4276.